ORIGINAL ARTICLE

Multi-objective optimization of solvent cast 3D printing process parameters for fabrication of biodegradable composite stents

Jasvinder Singh[1] · Gurminder Singh[2] · Pulak Mohan Pandey[1]

Abstract

A solvent cast 3D printing (SC-3DP) technique was explored comprehensively to fabricate bioresorbable polymer matrix composite stent in the present study. The developed methodology was assessed by printing the customized shape stent on the rotating mandrel. The polymeric composite was developed by blending bioresorbable carbonyl iron powder (CIP) and polycaprolactone (PCL). The process parameter's effect on percentage shrinkage in strut width and strut thickness, radial compression load and flexibility of stents was evaluated. Response surface methodology (RSM) was used for designing the experiments utilizing the process parameters like material compositions, printing speed and layer thickness. Analysis of variance was used to find out the significant parameters. The regression analysis was performed to obtain statistical equations with significant terms. It was noted that the reinforcement of CIP improved the fluidity of the material for better deposition as compared to pure PCL. The printing speed and layer thickness were observed to have a significant effect on the process. The significant interaction between layer thickness and printing speed parameters was also observed for shrinkage in width and thickness, compression and flexibility properties. Moreover, multi-objective optimization was performed using a genetic algorithm technique to minimize the percentage shrinkage of strut width and thickness, and load for bending to evaluate flexibility and maximize radial compression load. The method opens a unique way to fabricate patient-specific bioresorbable composite stents with customized properties.

1 Introduction

In current medical practices, bioresorbable stents are gaining attention to treat cardiovascular diseases and other vascular complexities [1]. Bioresorbable stents resorb after the restoration of a blocked artery leaving behind the healed and healthy natural blood vessel. After-effects of such stents may improve lumen gain, long-duration vascular rehabilitation and permanent healing [2, 3]. Consequently, the development of artificial vascular grafts leads to the fabrication of stents due to their excellent biocompatibility, biodegradability and drug loading capacity [4, 5]. In the family of bioresorbable materials,

polymeric materials are being preferred relative to their metallic counterparts. Various bioresorbable polymers such as polyglycolic acid (PGA), polylactic acid (PLA), poly(lactic-co-glycolic acid) (PLGA), polycaprolactone (PCL), polycarbonate (PC) and poly(butylene succinate) (PBS) have been successfully used for the fabrication of bioresorbable stents. Easy processability, controlled degradation rate and biocompatible PCL behaviour make it suitable for long-term vascular scaffolding and drug delivery inside the human body [6]. PCL is a semi-crystalline thermally stable polymer that exhibits excellent flexibility. It has lower tensile strength and low tensile modulus due to its semi-crystalline structure [6, 7]. The flexibility makes it permissible for easy deployment and, therefore, a suitable candidate for vascular stents. However, the fabrication ability of the PCL for the customized stents with sufficient mechanical properties is not adequate. Numerous micro- to nano-sized particles such as calcium carbonate ($CaCO_3$), calcium phosphates (CaPs), montmorillonite (MMT) and alumina (Al_2O_3) have been reinforced in PCL to improve the physical behaviour [8–11]. Gupta et al. [8]

✉ Gurminder Singh
Gurmindersingh2012@gmail.com; Gurminder.singh@ucd.ie

[1] Department of Mechanical Engineering, Indian Institute of Technology Delhi, New Delhi, India

[2] School of Mechanical and Materials Engineering, University College Dublin, Dublin, Ireland

developed a composite of PCL and TiO$_2$ (anatase and rutile) using the electrospinning process. The results showed that the interaction between polymer and anatase-type TiO$_2$ was significant, which resulted in the enhancement of mechanical characteristics. Vella et al. [12] analysed polycaprolactone composite behaviour by incorporating calcium phosphate in the PCL matrix and fabricated scaffold using 3D printing. The results concluded that improved toughness to fracture, strength in bending and modulus of flexural were observed. Among the micro-sized particles, carbonyl iron powder (CIP) is a pure form of iron that has a great potential to amend the mechanical properties of polymers [9, 13–16]. CIP has a good bioavailability in the human body [17]. The incorporation of CIP in polymer matrix resulted in the improvement of biocompatibility and non-thrombogenicity of the composite material [18]. Also, the increase in CIP (wt%) led to improved mechanical behaviour [19]. However, the fabrication of reinforced PCL as composite bioresorbable stents is challenging, especially for a specific patient.

Fabrication of a stent requires prior knowledge of selecting raw materials, stent designs, types of stents, fabrication methods and post-processing. Till now, techniques used to manufacture polymeric stents involve laser cutting, electrospinning, injection moulding and 3D printing [20–22]. The 3D printing technique has emerged as a useful method for the fabrication of stents. It gives an advantage for the fabrication of patient-specific stents [23]. The blockage information from CT/MRI scan data can estimate CAD design for the required strength and degradability period [24]. Various 3D printing techniques have been evolved including stereolithography apparatus (SLA) [25], selective laser melting (SLM) [26] and extrusion-based 3D printing such as fused deposition modelling (FDM) [27–29] and solvent cast 3D printing (SC-3DP) technique [30, 31]. Qiu et al. [32] fabricated a novel PCL stent by using the electrospinning-based 3D printing technique. Additionally, surface modifications of the stent were done by 2-*N*,6-*O*-sulfated chitosan (26SCS). The results concluded that surface modification of the stent enhanced the biological characteristics with no significant improvement in the mechanical properties. Jia et al. [33] fabricated a biodegradable polymeric stent from shape memory PLA using the hot-melt extrusion 3D printing process. In this study, mechanical behaviour such as longitudinal contraction and self-expansion studies was explored. Conclusively, PLA material showed a strong candidacy for the fabrication of shape memory stent by FDM. Xu et al. [34] fabricated a PLA biodegradable stent using a modified FDM-based 3D printer. The results indicated that a stent could be successfully implanted in the artery to open up the stenosis. However, the dimensions of the stents were expanded after the printing, which was attributed to poor dimensional accuracy. van Lith et al. [25] developed a technique based on stereolithography, named micro-continuous liquid interface production (μclip).

A bioresorbable stent was fabricated from a photocurable liquid resin with a better surface finish. However, the printing time was very high (~ 70 min) for a 20-mm-long stent due to the meagre printing speed (5 μm/s). The reduction of mechanical properties was observed at a higher scanning speed. Flege et al. [26] fabricated a coronary stent prototype from bioresorbable polymers by utilizing SLM. The high-temperature requirement for fabrication resulted in reduced biological properties by lowering the level of human arterial smooth muscle cells on the PCL surface. Also, degradation products produced inflammatory responses under in vivo conditions. Zhao et al. [4] developed a polymeric stent on a homemade 3D printing system working on the FDM technique having a rotating coordinate axis in addition to the primary three coordinate axes. Printed parts required post-processing for the removal of hanging fibres and overflow filaments. The techniques had a limitation of the thermal degradation of material undergoing the melt extrusion [30]. Among these 3D printing techniques, SC-3DP can be utilized as an effective stent fabrication technique due to its low fabrication time and non-heated biomaterial ink, which can preserve material bioactivity. Also, the processing cost of SC-3DP is low as compared to that of other 3D printing techniques. A variety of polymers and inorganic substances can be dissolved in the polymer solution to customize composite ink properties for SC-3DP [30]. Dichloromethane (DCM), acetone, dimethylformamide (DMF) and chloroform are highly volatile solvents that are extensively used in SC-3DP. Many of the researchers have developed customized ink for SC-3DP such as poly-L-lactic acid/DCM, polyvinylidene fluoride (PVDF)/DMF/acetone and polysulfone/DCM/DMF [30, 35, 36]. In SC-3DP, the bioactivity of materials retains, making the technique suitable for cell seeding and culturing in tissue engineering applications [30, 35]. However, the printing of the cardiovascular stents on a flat substrate with the SC-3DP technique is challenging as stents have many interconnected mesh structures. Therefore, the development of SC-3DP with the cylindrical substrate can overcome these difficulties.

Based on the literature, PCL was determined to be the best material for the fabrication of bioresorbable polymer stents. Also, the reinforcement in PCL is an effective method to overcome the low mechanical properties of PCL. SC-3DP is the emerging technique of 3D printing, which gives the advantage to print any polymer or polymer composite material. However, this method is challenging in use to fabricate cylinder shape stents with interconnected design shells. Also, the FDM technique used with cylindrical mandrel opens a unique way of fabricating stents. Therefore, in the present study, the SC-3DP technique is combined with print on the cylindrical mandrel method to print PCL-CIP–based bioresorbable stents. The developed method is explored for two primary responses: accurate printed dimensions, namely strut width and thickness, and mechanical properties of the stents, precisely radial

compression and bending loads. The processing parameters were selected as printing speed, layer thickness and material composition. Response surface methodology (RSM) is based on the design of experiments and is used to investigate the effects of process parameters on individual and interaction responses. The genetic algorithm–based multi-objective optimization has been performed to minimum geometry shrinkage compared to CAD models and maximizes the mechanical properties.

2 Materials and methods

2.1 Materials

The printing material for SC-3DP was prepared by using PCL polymer (Sigma-Aldrich, Mn = 80,000), DCM (Fisher Scientific, minimum assay = 99.5%) and CIP (BASF Germany, CN grade, 99.5% pure iron).

2.2 Material preparation

The polymeric composite materials (PCL-CIP) were prepared by reinforcing the variable weight percentage of CIP, ranging from 0.5 to 2.0% in the PCL matrix. Initially, PCL was dissolved in DCM for 24 h in an airtight glass bottle. Separately, CIP was added to another glass bottle and stirred in the ultrasonic bath for 1 h. Both the solutions were mixed together by rigorous mechanical stirring for the next 1 h. Further, the prepared composite material was fed into the syringe, and the syringe was mounted to the printhead for printing. The ratio of 3:1 for DCM:PCL was used for preparing five different material samples by varying the weight percentage of CIP in the PCL as 0%, 0.5%, 1.0%, 1.5% and 2%. Hence, the prepared CIP-reinforced PCL composites were further used for the printing of bioresorbable stents. The composite samples with CIP percentages ranging from 0 to 2% were labelled PC, PCF0.5, PCF1, PCF1.5 and PCF2, respectively.

2.3 Proposed methodology

The stent fabrication in the present study was based on the novel developed methodology, as shown in Fig. 1a. The 3-axis machine was used to fabricate the required shape of the tubular scaffold. The g-code of the sliced CAD model was imported to the printer for fabrication.

A 3-axis 3D printing machine based on the SC-3DP technique is shown in Fig. 2. With the coordination of machine components such as rotating mandrel, stepper motor and printhead, polymer composite stents were fabricated. The stents were easily fabricated with the printhead controlled movement, governed rotation of mandrel, the flow of material through nozzle and deposition of material on rotating mandrel.

The length and thickness of the stents were maintained by controlling the motion of the x-axis and z-axis. However, the circumference of the stent was built by the governed rotation of the mandrel along the y-axis. The material was extruded through the nozzle and directly deposited on the mandrel during printing, as shown in Fig. 2. The material flow was controlled with the help of the dispensing gear attached to the printhead. Apart from the mentioned controls, some other attachments (coupling, BD 10-ml syringe, dispensing tip) were also implemented to facilitate the fabrication of the stent. The purpose of the coupling was to connect the mandrel to the stepper motor. The prepared material was filled in the BD 10-ml syringe, which was extruded through the dispensing tip.

A freeware CURA software program was generated by a g-code of linear stent model, as shown in Fig. 3. The stents were successfully printed only by a 22-G-sized nozzle, as observed in pilot experiments. The layer thickness, printing speed and material compositions were selected as the process parameters to fabricate the stent. Hence, the printing of the stent was done on the rotating mandrel by SC-3DP.

2.4 Stent model

The fundamental unit of a stent is a strut, which provides radial support during implantation, and geometrical attributes determine the performance [37]. Therefore, a CAD model of the diamond-shaped stent was designed with dimensional parameters such as inner diameter, strut width and strut thickness, as shown in Fig. 1. The stent shape was based on the laser-cut self-dilating nitinol stent developed to assess stent arterial interaction [38]. The physical and biological behaviour of the stent directly depends upon these parameters. In this work, the stent was modelled as per the intravascular ultrasonic (IVUS) guidance, i.e. inner diameter and length ranged from 2.4 to 4 mm and from 8 to 38 mm, respectively [39]. Figure 1b shows a stent model with designed geometrical features having an inner diameter, length, strut width and strut thickness equal to 3 mm, 30 mm, 0.5 mm and 0.3 mm, respectively.

2.5 Measurements of responses

The percentage shrinkage in strut width and strut thickness was calculated using the following formula:

$$\text{Shrinkage in strut width } (\%), w_s = \left(1 - \frac{w}{w_c}\right) \times 100 \quad (1)$$

$$\text{Shrinkage in strut thickness } (\%), t_s = \left(1 - \frac{t}{t_c}\right) \times 100 \quad (2)$$

where w_c and t_c are the strut width and strut thickness of the CAD model, respectively, and w and t are the measured values of strut width and strut thickness, respectively. The calibrated

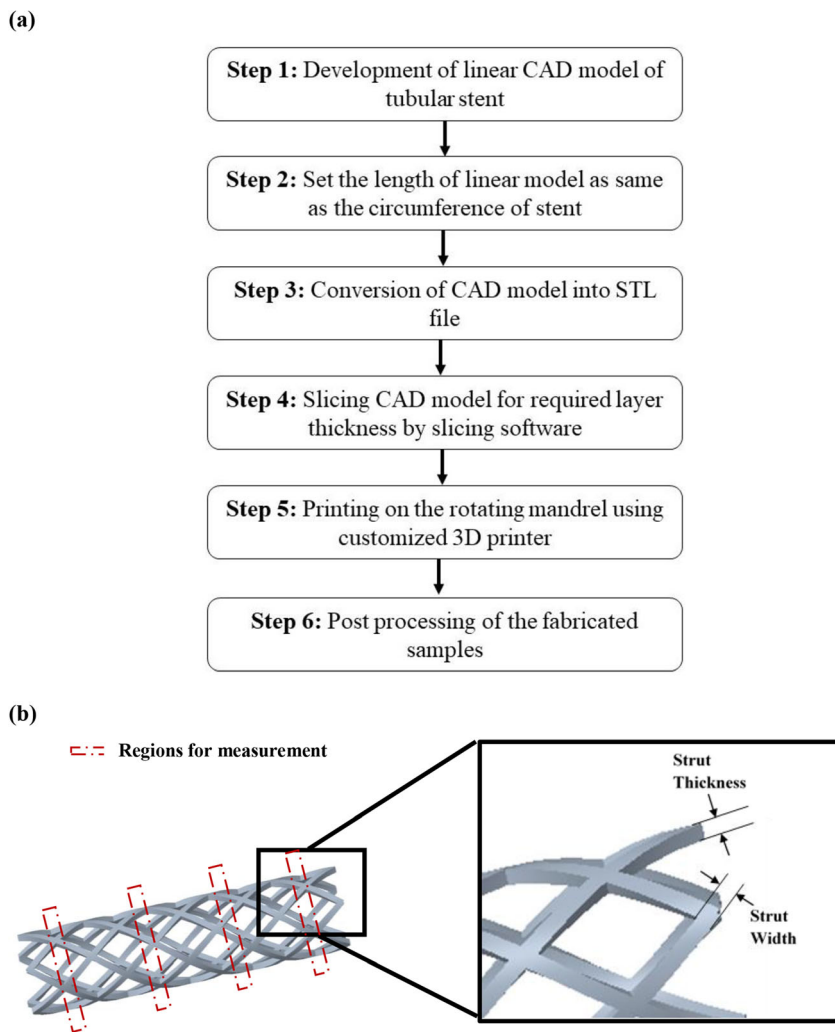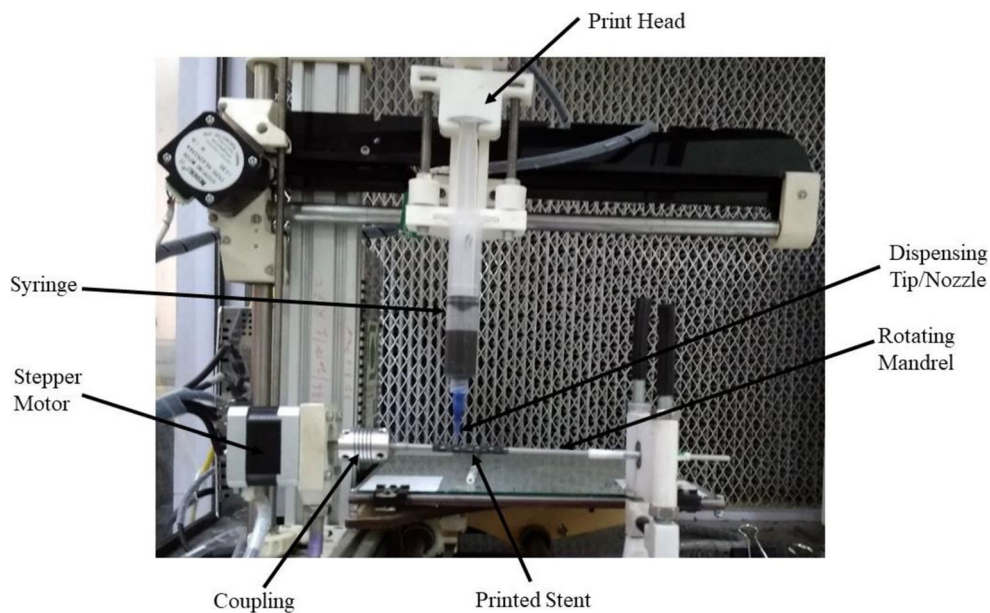**Fig. 1** **a** Flowchart of the proposed methodology. **b** Stent geometry

(a)

Step 1: Development of linear CAD model of tubular stent

↓

Step 2: Set the length of linear model as same as the circumference of stent

↓

Step 3: Conversion of CAD model into STL file

↓

Step 4: Slicing CAD model for required layer thickness by slicing software

↓

Step 5: Printing on the rotating mandrel using customized 3D printer

↓

Step 6: Post processing of the fabricated samples

(b)

⌐¦⌐ **Regions for measurement**

Strut Thickness

Strut Width

Fig. 2 Setup of the solvent cast 3D printer with a rotating mandrel

Print Head

Syringe

Stepper Motor

Coupling

Printed Stent

Dispensing Tip/Nozzle

Rotating Mandrel

digital microscope (Dinolite v2.0) was used for measurement, and mean values of w_s and t_s were calculated from three repeated samples. This method has been adopted by several authors to measure small feature dimensions [40–42]. The calibration of the digital microscope was done by using a standard scale provided by the manufacturer. After the calibration, strut width and strut thickness were measured at sixteen different locations on the specimens. Four points were measured at four different regions, as shown in Fig. 1. The points were chosen to have a homogenous measurement on the stent and to make the results more robust. Thereafter, the average of the measured values was calculated along with the standard deviation. In the present experimentation, radial compression load (R_L) was measured by parallel disc radial compression test. A universal testing machine (UTM) (Shimadzu AG-X series) was used for radial compression test at a load movement of 1 mm/min as per the ISO 25539-2 [43]. The bending load (F_L) was measured by a 3-point bending examination, which is the simplest method to determine the flexibility of stents [16]. In conformance with standard ASTM F2606, a UTM (Shimadzu AG-X series) for a 3-point bending test was used with a span length of 15 mm and at the loading rate of 1 mm/min [44]. The test was performed to the constant displacement of 1.5 mm for all experiments to measure the bending load and to check the flexibility of the fabricated stents. The mechanical tests were performed on three repeated samples, and the average of the data was used. The SEM images of the fabricated samples were captured using SEM (Zeiss EVO 50 Special). The EDX machine (Hitachi High Technology) was employed to study the element contribution of the element and the mapping. The rheology of prepared composite materials was investigated at 25 °C on an Anton Paar 302 rheometer using parallel plate geometry of a diameter of 25 mm.

2.6 Preliminary experimentation

The effect of process parameters on the prior mentioned process responses was studied by performing the preliminary experimentation on SC-3DP. The experiments were performed to primarily evaluate the percentage shrinkage in the strut width and strut thickness. Table 1 represents the process parameters followed up in the initial experimentations.

Figure 4 represents the effect of the layer thickness and printing speed on the w_s and t_s in SC-3DP. It is evident from Fig. 4 that w_s and t_s were increased with the increment of layer thickness and printing speed. The increase in the percentage shrinkage could be attributed to the dragging effect, gravity at higher printing speed and increased layer thickness [4]. The increase in layer thickness resulted on the account of the significant gap between the nozzle tip and substrate. The increasing gap led to the dragging of the filament. The dragged filament had a reduced cross-sectional area which resulted in
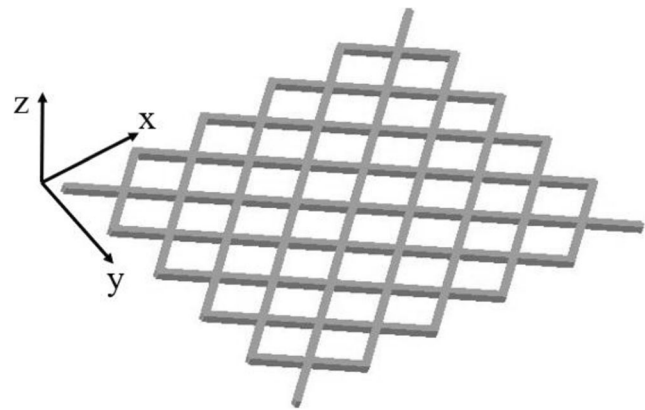

Fig. 3 Linear CAD model of the stent

percentage shrinkage [45]. The dimensions shrank as the printing speed increased due to filament stretching. This enhanced the evaporation rate of the solvent and caused a shrinkage in dimensional attributes of the stent [46]. The reasons behind the overall deviation in the dimensions of strut width and strut thickness were attributed to the dragging effect, the gap between dispensing tip and substrate, reduction in the cross-sectional area of extruded filament, stretching of the filament and increased evaporation rate.

2.7 Designing of experiments

The preliminary experiments significantly disclosed the strut width and strut thickness variation with a change in the printing speed and layer thickness. However, in previous research, the change in the mechanical properties due to variation in the layer thickness and print speed was reported [47–51]. Hence, the selection of process parameters such as layer thickness and printing speed were based on their significant effect on shape fidelity in the pilot works. Another factor of material composition was selected based on the effect of variable material composition on the 3D printed part's mechanical behaviour in the previous study [19, 52, 53]. The experimentations were designed as a central composite design (CCD). The method helps to design systematic experiments with the minimum number of runs and a wider range of the parameters [53, 54]. Moreover, the deviation of the dimensional attributes and the mechanical behaviour of printed stents were studied. The study involved the application of RSM to analyse the process parameters for efficient printing of the stent. The response surface equation can be represented as a second-order polynomial as

Table 1 Process parameters in the preliminary experimentation

CIP (%)	1 wt%
Print speed	5–25 mm/s
Layer thickness	0.1–0.3 mm

(a)   **(b)**
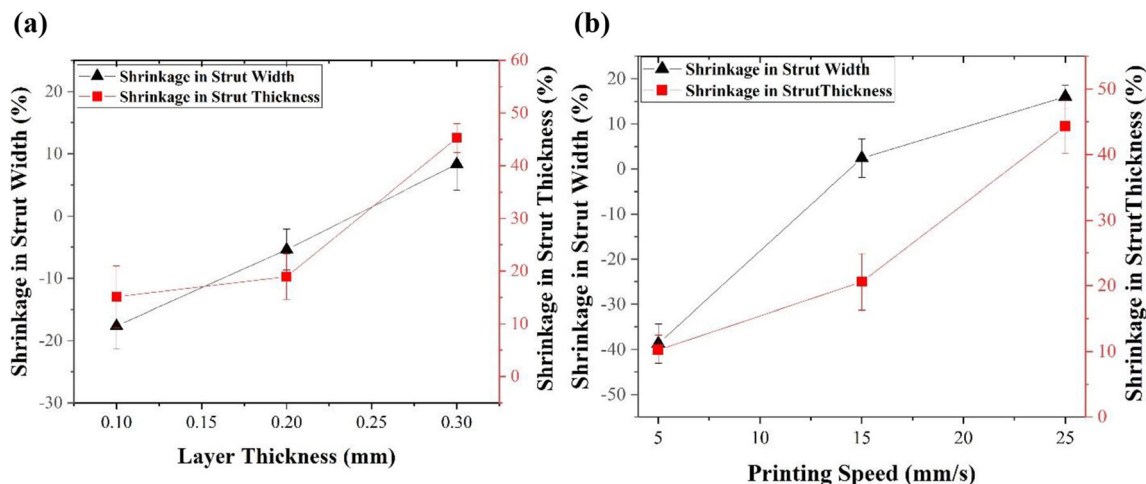
Fig. 4 Percentage shrinkage in strut width and strut thickness in relation to **a** layer thickness and **b** printing speed

$$Y(\mathbf{X}) = \alpha_0 + \sum_{i=1}^{k} \alpha_i Z_i + \sum_{i=1}^{k} \alpha_{ii} Z_i^2 + \sum_{i<j}^{k} \alpha_{ij} Z_i Z_j + \varepsilon \qquad (3)$$

where K is the number of parameters; α_0, α_i, α_{ii} and α_{ij} are the parameter-depending constants with ε a random error; and Z_i, Z_i^2 and $Z_i Z_j$ are the first order, the second order and the interaction terms for the process parameters, respectively. For the present study, $K = 3$ for the four different responses. The range of variations occurring in the responses was evaluated by Eq. (4).

$$Y_{\mathrm{r}} = Y_{\mathrm{p}} + t_{\frac{\alpha}{2},DeF} \times \sqrt{V_{\mathrm{e}}} \qquad (4)$$

where Y_{r} describes the ranges of responses, Y_{p} represents the predicted values of responses from the formulated regression models, $t_{\frac{\alpha}{2},DeF}$ represents the t value with a significant level $\frac{\alpha}{2}$ and degree of freedom (DeF) and V_{e} refers to the variance of observed error in the prefigured model. The confidence level of 95% in analysis of variance (ANOVA) was also considered to evaluate significant terms and assess the error range. The different levels of the parameters for the design of experiments are shown in Table 2.

3 Results and discussions

3.1 Experimental runs and statistical analysis

The method of SC-3DP with rotating mandrel was successfully developed to fabricate bioresorbable stents, as shown in Fig. 2. The success of the methodology was evidenced by the fabrication of different designs of the stent, as shown in Fig. 5. The method was also able to fabricate other similar designs as per the CAD model. However, shrinkage was observed in strut thickness and width. Therefore, the study of parameters and their optimization was performed to improve the efficacy of the method. For this study, a stent design based on the laser-cut self-dilating nitinol stent as per IVUS guidance was fabricated [55].

Figure 6a shows the diamond-shaped polymer stent (PC) and polymer composite stent (PCF1), respectively. The proposed methodology was effective in the fabrication of pure polymer and polymer composite stents. Hence, material selection would not be a constraint for the proposed methodology of stent fabrication. Moreover, EDX analysis was performed to verify the involvement of the CIP in the polymer matrix (ref. Fig. 6b). Table 3 shows the wt% of the elements observed on the entire surface of a strut. The presence of carbon (C) and

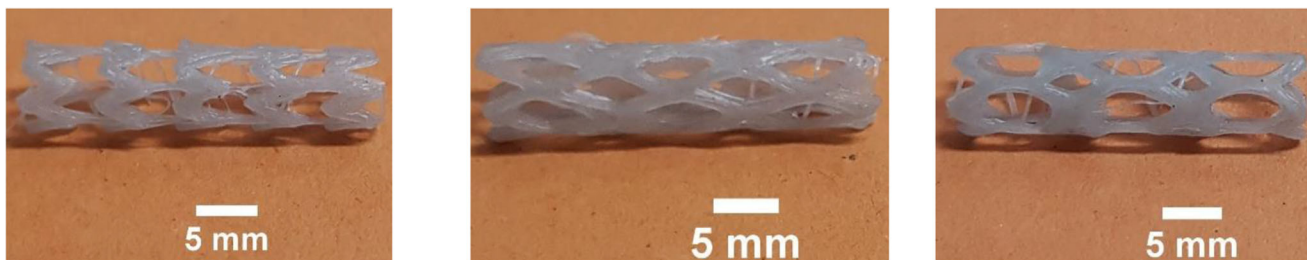| Table 2 Printing parameters with defined levels	Symbols	Process parameters	Levels				
			−2	−1	0	+1	+2
	Z1	Printing speed (mm/s)	4	8	12	16	20
	Z2	Layer thickness (mm)	0.1	0.15	0.2	0.25	0.3
	Z3	Material compositions (% CIP in PCL)	0	0.5	1.0	1.5	2.0

Fig. 5 Different geometries of the stents fabricated by the proposed methodology

oxygen (O) corresponds to the PCL polymer chain, and iron (Fe) in composite materials corresponds to CIP. The presence of C and O corresponds to the PCL polymer chain, and Fe in composite materials corresponds to CIP. The Fe wt% was increasing with an increase in CIP percentage, and values were nearby to the material composition parameter levels (Z_3). Any foreign material other than PCL and Fe was not involved in the matrix, as revealed from the EDX analysis. Hence, the fabricated polymer and polymer composite stents were free from any type of contamination.

The schematic diagram of CIP reinforcement in PCL is shown in Fig. 6d. In general, the blending of the foreign materials in the PCL matrix results in the reinforcement [56, 57]. It was found from previous researches that PCL formed a stable hydrolytic composite [56]. Also, it displayed a good physical interaction with the foreign materials, which resulted in the development of reinforced composite [57]. Also, the addition of CIP could increase the mechanical properties and provide better 3D printing fluidity characteristics, which are discussed further. The rheological characterizations were evaluated for the flow properties of the material under the applied shear strain rate. The apparent viscosity was calculated as a function of shear rate (1–80) for all the composites prepared, as shown in Fig. 7. Pure PCL and PCL-CIP composites exhibited a shear thinning behaviour, indicating an excellent flow behaviour of the material for extrusion as the viscosity of composite materials decreased as a function of shear rate [58]. Thus, the developed SC-3DP printing was used to fabricate PCL and PCL-CIP composite stents. However, the printing parameter affects the printing quality and the mechanical properties of the fabricated stents. The statistical analysis

of the printing parameters was conducted as per the RSM method described earlier.

The responses calculated as per RSM experimental runs are shown in Table 4. The obtained response data for w_s, t_s, R_L and F_L were investigated using ANOVA. Tables S1–S4 represent the ANOVA results for w_s, t_s, R_L and F_L with significant terms ($P < 0.05$), respectively. The second-order regression equations for the response variables were obtained through the regression analysis. The regression equations in terms of variables are presented in Eqs. (5)–(8).

$$w_s = -43.3 - 16.52 \times Z_1 + 3.82 \times Z_2 - 25 \times Z_3 + 7.24$$
$$\times Z_1^2 + 0.1140 \times Z_2^2 + 903 \times Z_3^2 - 18.98 \times Z_2$$
$$\times Z_3 \tag{5}$$

$$t_s = -45.3 - 14.27 \times Z_1 + 5.15 \times Z_2 + 81 \times Z_3 + 6.25$$
$$\times Z_1^2 + 572 \times Z_3^2 - 16.37 \times Z_2 \times Z_3 \tag{6}$$

$$R_L = 4.266 + 1.909 \times Z_1 - 0.1221 \times Z_2 + 4.17$$
$$\times Z_3 - 0.753 \times Z_1^2 - 0.00568 \times Z_2^2 - 43.4 \times Z_3^2$$
$$+ 0.609 \times Z_2 \times Z_3 \tag{7}$$

$$F_L = 1.462 + 0.4863 \times Z_1 - 0.0702 \times Z_2 + 0.57$$
$$\times Z_3 - 0.1976 \times Z_1^2 - 10.87 \times Z_3^2 + 0.1758 \times Z_2$$
$$\times Z_3 \tag{8}$$

The developed statistical models were validated by performing the confirmatory experiments as represented by Table 5. The results inferred that observations were in conformity with the statistically developed models.

3.2 Effect of process parameters on w_s and t_s

Figure 8 and Fig. 9 represent the various effects and percentage contribution of the significant process parameters on w_s and t_s of the printed stents, respectively. The w_s and t_s were varied from −20 to +30% and from −10 to +20%. The negative sign indicated the expansion of the dimensions. The printing speed and layer thickness were more effective
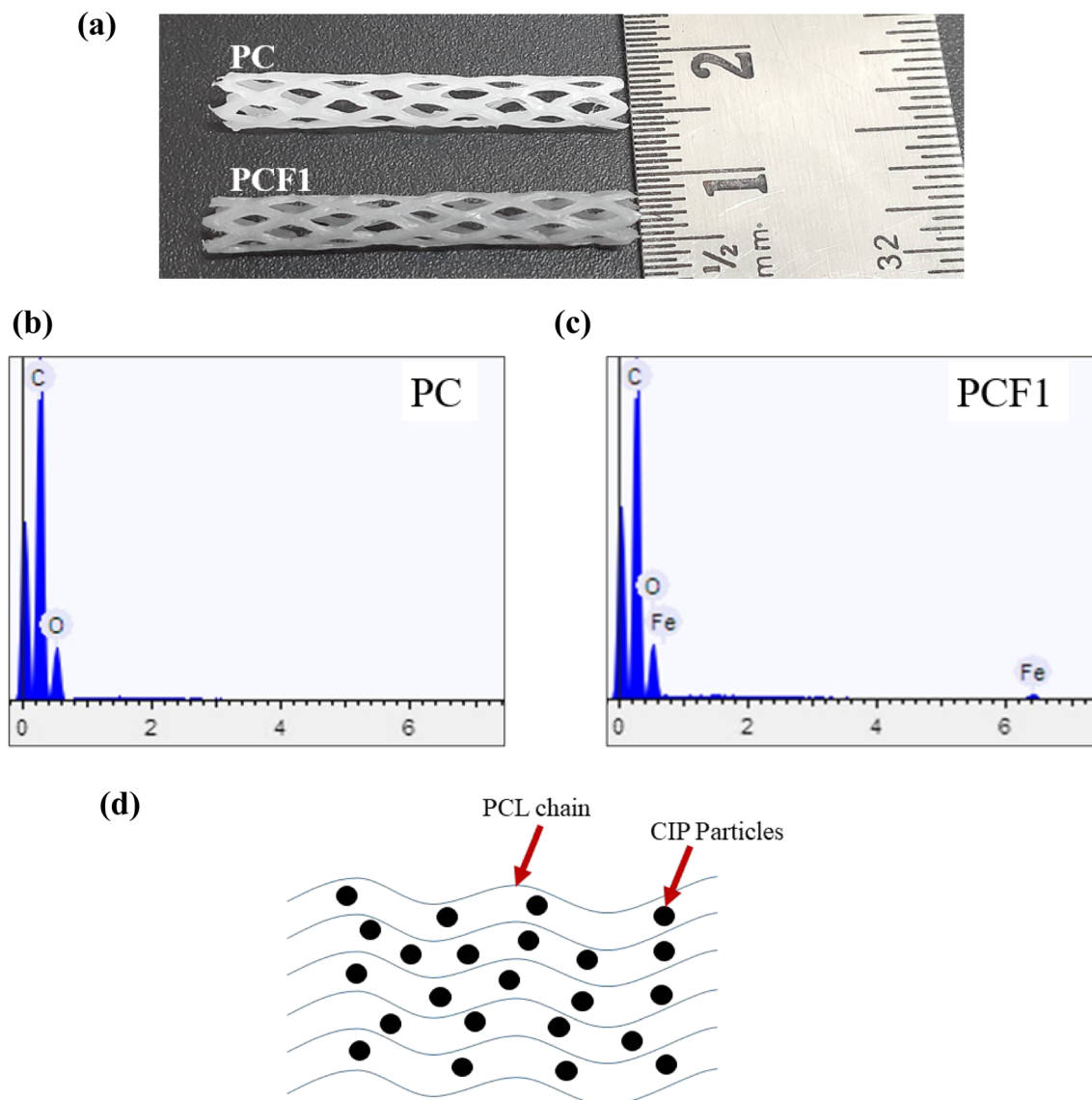
Table 3 Elemental details of the prepared samples observed in EDX analysis

Samples	C (wt%)	O (wt%)	Fe (wt%)
PC	69.189	30.811	0
PCF0.5	68.664	30.838	0.498
PCF1	68.637	30.358	1.006
PCF1.5	68.577	29.868	1.555
PCF2	68.594	29.433	1.968

Fig. 6 **a** PC stent and PCF1 stent printed by SC-3DP on the proposed methodology. EDX analysis of **b** PC and **c** PCF1 stents. **d** Schematic representation of CIP reinforcement in PCL

parameters than the material composition. The following segments describe the effects of individual process parameters upon the strut width and strut thickness.

3.2.1 Effect of material compositions

The variation of the CIP (%) in the PCL matrix resulted in an insignificant effect on w_s and t_s, as shown in Fig. 8 and Fig. 9. The average density of the PCL blend was increased by mixing CIP. The rise in the density was due to different densities of filler material [59]. PCL (1.14 g/cm^3) has a less density in comparison to the iron (7.5 g/cm^3) [59, 60]. Also, it had been observed that the addition of the filler material in the PCL led to an increase in the density [59]. The reinforced particles provided better fluidity during printing and, thus,

decreased the shrinkage as compared to pure PCL as shown in Fig. 9. The improvement in the fluidity could be attributed to the shear-thinning behaviour of the materials. Huang and Bártolo [61] obtained a similar kind of results in which shear thinning behaviour was increased with an increase in the ceramic percentage in the polymer matrix. However, insignificant changes in the dimensions were observed with an increase in the percentage of CIP in the composite.

3.2.2 Effect of layer thickness

The variation of the dimensions in the strut width and thickness was changed from expansion to shrinkage with the increase in layer thickness. The printed part with a lower thickness value of 0.1 mm was having an overdeposition of material due to the
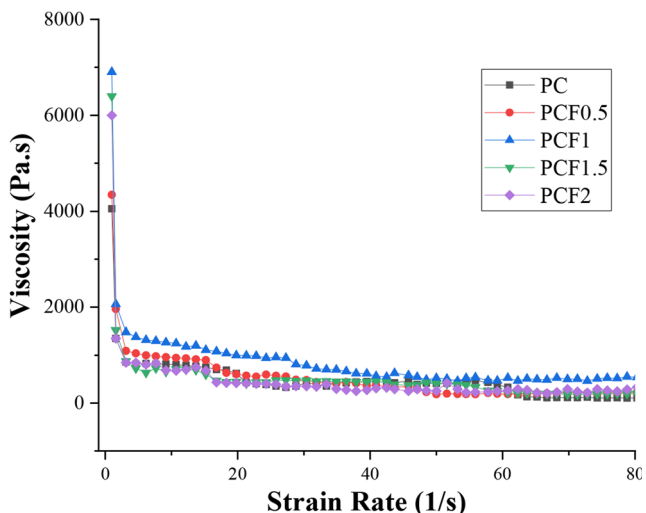
Fig. 7 Viscosity as a function of strain rate for PC, PCF0.5, PCF1, PCF1.5 and PCF2

material constant extrusion rate [62]. The layer-by-layer bonding mechanism in SC-3DP is generally based upon solidification of the polymer by evaporation of the solvent. There was a tiny space for the evaporation of the solvent due to the less gap between the nozzle and rotating mandrel in terms of small layer thickness (0.1 mm). Therefore, strut thickness and width dimensions resulted in expansion with small layer thickness. The increase in the dimensions was justified by a negative value in the shrinkage parameter. The more significant gap between nozzle and mandrel resulted in better evaporation of the solvent.

Therefore, at 0.2-mm layer thickness, the shrinkage was approximately zero. However, the higher value of shrinkage was noticed at 0.3 mm of layer thickness due to the dragging effect. Furthermore, the cross-sectional area and diameter of the filaments were reduced because of dragging, which led to an increase in solvent evaporation rate. Hence, shrinkage was observed in both geometrical attributes (strut width and thickness) at the layer thickness of 0.3 mm. A similar kind of variation concerning layer thickness was noticed by Jin et al. [45].

3.2.3 Effect of printing speed

Printing speed showed a pronounced impact on the dimensional values of the strut width and strut thickness, as described in Fig. 8 and Fig. 9. The shrinkage percentage was increased with increasing the printing speed. Generally, the accumulation of extruded material is affected by the printing speed. At a lower value of 4 mm/s, the material deposition was more in comparison to the printing speed of 20 mm/s due to the constant flow of the material. Therefore, oversized dimensions were produced at a lower printing speed [63]. Further, filament stretching was observed during printing at 20 mm/s, which resulted in the reduction of filament diameter. Thus, reduced filament diameter resulted in the shrinkage of strut width and thickness. Guo et al. [46] also noticed a similar effect of speed on the printing performance. Hence, constant extrusion speed and the constant volumetric flow rate

Table 4 Input process parameters with experimental responses

Exp. No.	Z_1 (%)	Z_2 (mm/s)	Z_3 (mm)	w_s (%)	t_s (%)	R_L (N)	F_L (N)
1	0.5	8	0.15	−18.27	−3.47	4.07	1.15
2	1.5	8	0.15	−19.72	−3.87	4.25	1.17
3	0.5	16	0.15	7.79	15.93	2.65	0.80
4	1.5	16	0.15	8.53	14.95	3.21	0.84
5	0.5	8	0.25	−1.44	13.93	3.34	0.94
6	1.5	8	0.25	−2.68	13.23	3.54	0.97
7	0.5	16	0.25	9.22	19.36	2.39	0.66
8	1.5	16	0.25	10.60	19.82	3.01	0.84
9	0	12	0.2	8.53	17.83	2.54	0.71
10	2	12	0.2	0.66	11.60	3.37	0.94
11	1	4	0.2	−20.00	−6.67	4.54	1.27
12	1	20	0.2	29.29	28.21	2.15	0.69
13	1	12	0.1	−6.02	2.16	3.98	1.11
14	1	12	0.3	18.78	26.21	2.58	0.72
15	1	12	0.2	−6.58	8.13	3.79	1.05
16	1	12	0.2	1.69	1.95	3.74	1.04
17	1	12	0.2	−5.39	8.00	3.90	1.09
18	1	12	0.2	−8.45	11.36	3.57	0.97
19	1	12	0.2	−0.62	4.34	3.77	1.05
20	1	12	0.2	−4.52	11.94	3.45	0.96

Table 5 Experimental confirmations

S. No.	Z_1	Z_2	Z_3	w_s (%)		t_s (%)		R_L (N)		F_L (N)	
				Statistical	Experimental	Statistical	Experimental	Statistical	Experimental	Statistical	Experimental
1	2	8	0.2	-8.77 ± 8.18	-9.13	5.24 ± 5.15	5.03	3.80 ± 0.33	3.57	1.04 ± 0.10	1.01
2	1	8	0.15	-20.93 ± 8.18	-18.39	-6.74 ± 5.15	-7.18	4.46 ± 0.33	4.24	1.24 ± 0.10	1.17
3	2	12	0.1	-1.37 ± 8.18	-1.62	7.13 ± 5.15	9.22	3.50 ± 0.33	3.26	0.96 ± 0.10	0.91

produced a shortened strut width and thickness at higher printing speed [64].

3.2.4 Effect of interactions

The surface 3D and line 2D interaction plots for w_s and t_s are shown in Fig. 10 and Fig. 11, respectively. It was observed that

high printing speed with small layer thickness showed a more significant effect on w_s and t_s as compared with large layer thickness. The number of layers in the fabrication of stent was less using large layer thickness, which resulted in higher shrinkage [49]. The phenomenon of overdeposition with low printing speed and small layer thickness increased the dimensions of strut width and strut thickness. However, at high printing speed and small

Fig. 8 a Main effects plot. b Percent contribution of each process parameter on percentage shrinkage in strut width
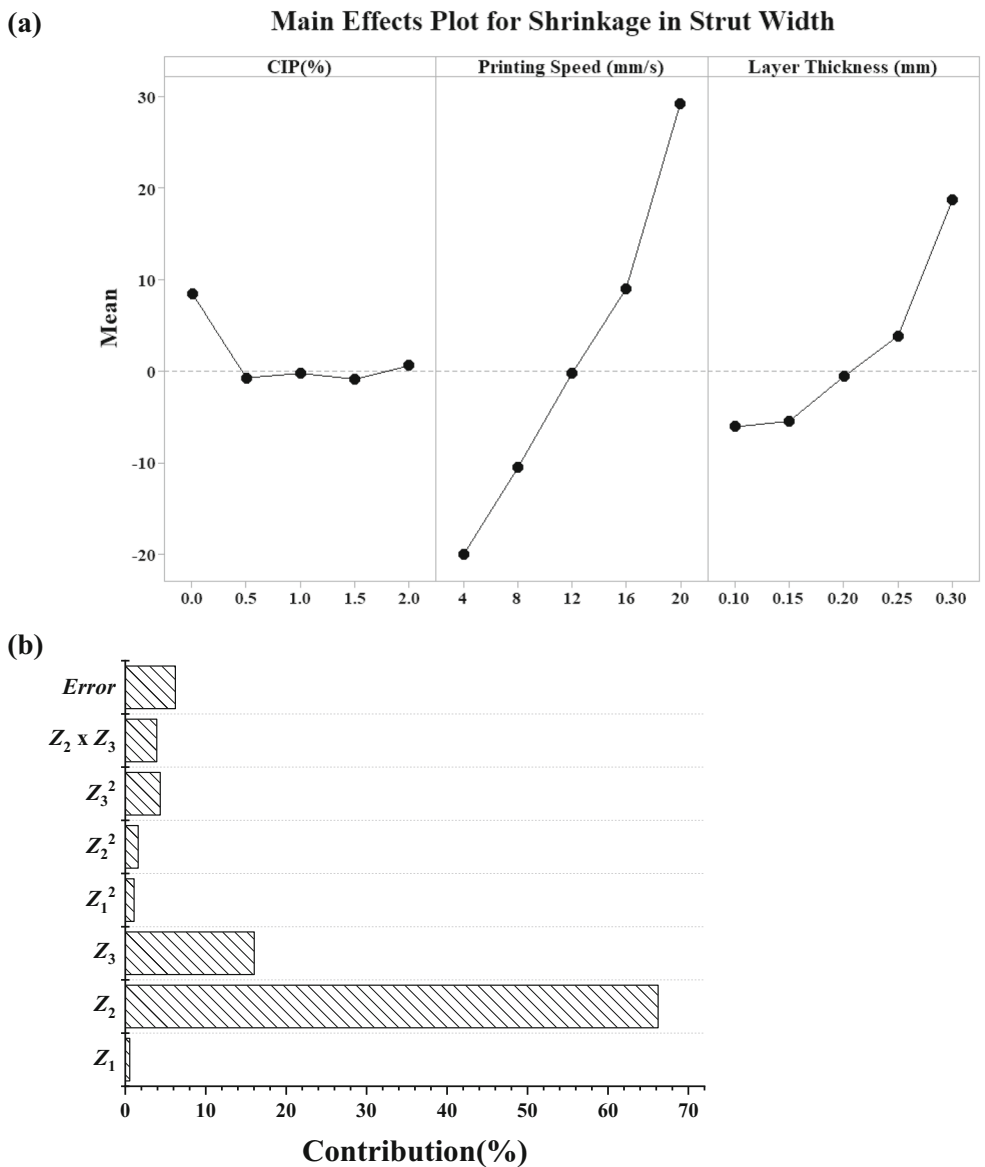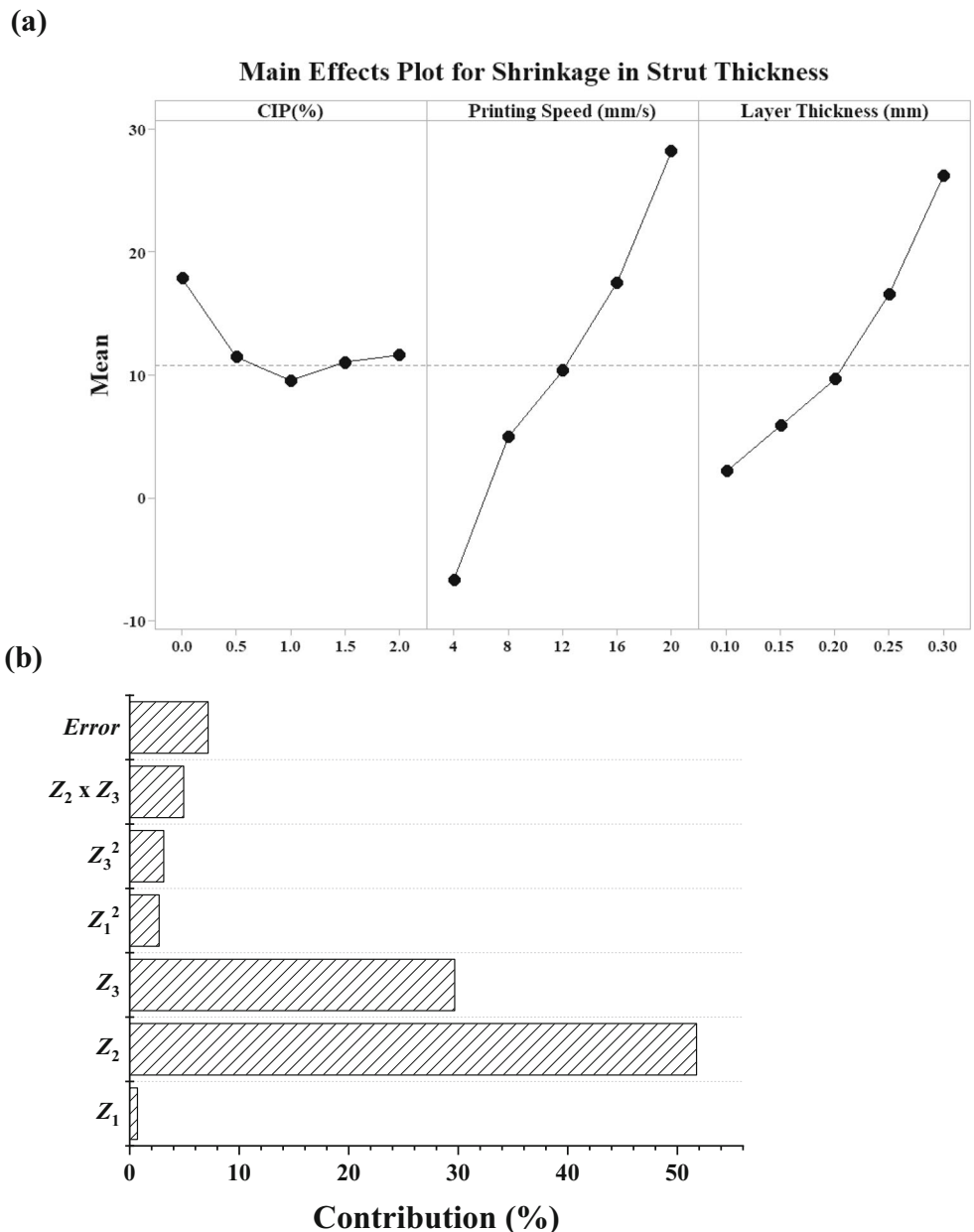

(a) **Main Effects Plot for Shrinkage in Strut Width**

(b)

Fig. 9 a Main effects plot. **b** Percentage contribution of each process parameter on percentage shrinkage in strut thickness

3.3 Effect of process parameters on R_L and F_L

Figure 12 and Fig. 13 depict the main effect of significant parameters and percentage contribution on the radial compression load (R_L) and flexural bending load (F_L) of the printed stents, respectively. All process parameters such as CIP (%), printing speed and layer thickness substantially affected R_L and F_L. The following subsections describe the effect of individual process parameters.

layer thickness, w_s and t_s were higher than the large-sized layer thickness and high printing speed because the filament stretching was higher than the small-sized layer thickness at a larger value of printing speed [4, 31].

3.3.1 Effect of material compositions

The reinforcement of CIP in polymer enhanced the mechanical properties of the composite material [9, 65]. The dispersion of CIP in the PCL matrix increased the strength of the composite stent samples PCF0.5 and PCF1 (ref. Figs. 12a and 13a). However, only small wt% of CIP acts as reinforcement to increase the mechanical properties. It could be attributed to the better dispersion of the filler materials with low wt% in the matrix [66]. Thus, the values of R_L and F_L were observed to increase up to 1 wt% of CIP. However, R_L and F_L values were decreased with increasing the wt% of the CIP beyond 1%. The high wt% of CIP resulted in the agglomeration of the metal particles in a polymer matrix which led to improper dispersion
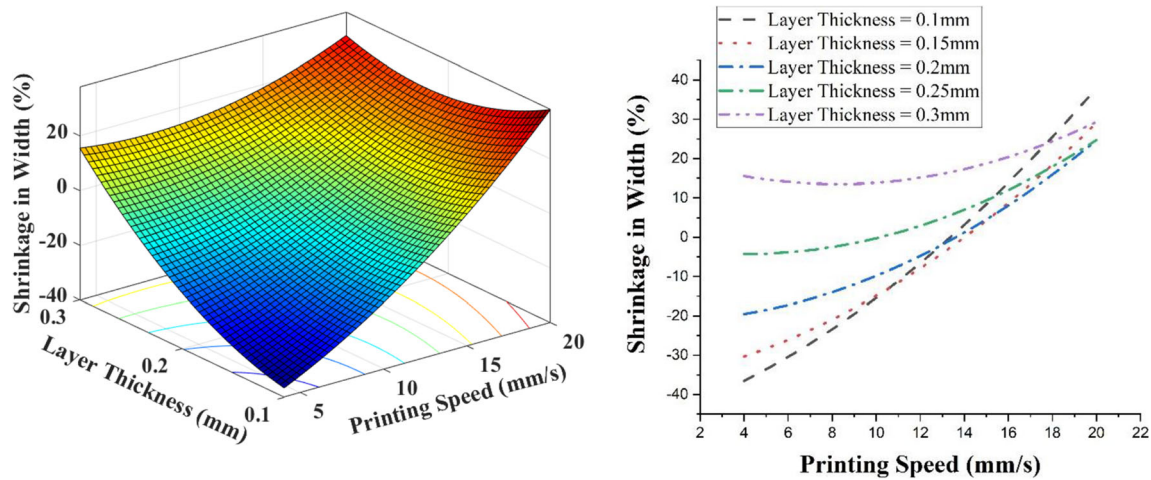
Fig. 10 Printing speed and layer thickness interaction plot on the percentage shrinkage in strut width

and generated stress concentration points [19, 67]. The agglomeration of CIP in printed parts for PCF1.5 and PCF2 can be easily observed in Fig. 14. The increase in the points of stress concentration resulted in early fracture during the mechanical test and directly reduced the strength [19]. Similar effect of iron material reinforcement in PCL for the mechanical properties was investigated by De Santis et al. [68].

3.3.2 Effect of layer thickness

In 3D printing, the improvement of mechanical characteristics also depends upon the layer thickness parameter. The lowest value of layer thickness resulted in maximum compression and flexural strength for the present study (ref. Figs. 12a and 13a). The low value of layer thickness results in a large number of layers which provides better interfacial strength between the layers due to compactness [49, 69]. This resulted in formation of small-sized voids between the layers as

compared to the parts printed with a high value of layer thickness [28]. The mechanical properties decreased with increasing the layer thickness value. The shrinkage in strut width and strut thickness in the parts printed with 0.3 mm of layer thickness reduced material quantity per unit area, which was also responsible for poor mechanical properties [26, 43].

3.3.3 Effect of printing speed

Usually in FDM 3D printing, the printing speed, i.e. the relative speed between the printing nozzle and the platform, is high between 40 and 100 mm/s. However, the high speed is not suitable for solvent casting printing especially for mechanical properties of the samples. Also, the PCL mixed with solvent for extrusion printing has high viscosity as compared to other FDM printed materials. The fast speed would reduce the extrusion volume of the material and provide poor printing stability [70]. The variation effect of printing speed from 4 to 20 mm/s on R_L and F_L is shown in Figs. 12a and 13a.
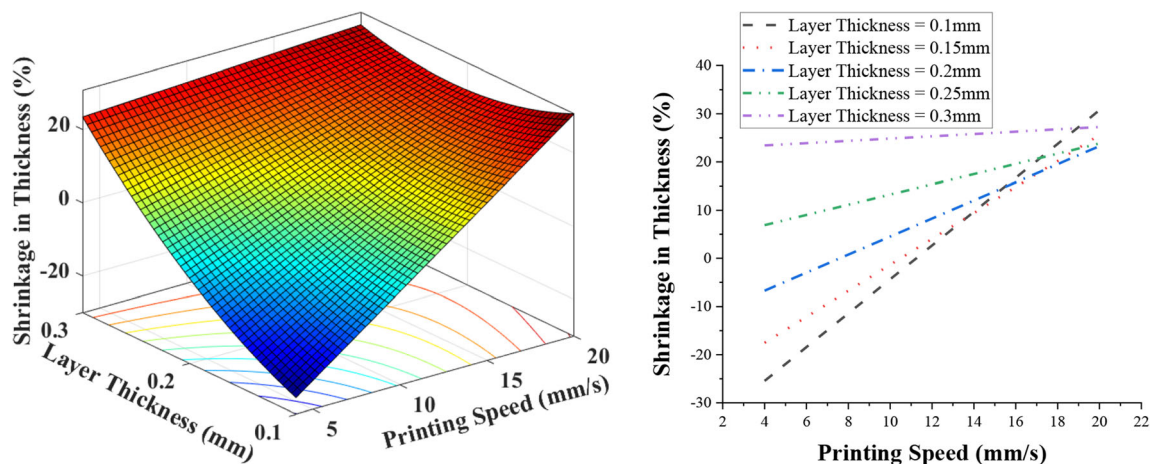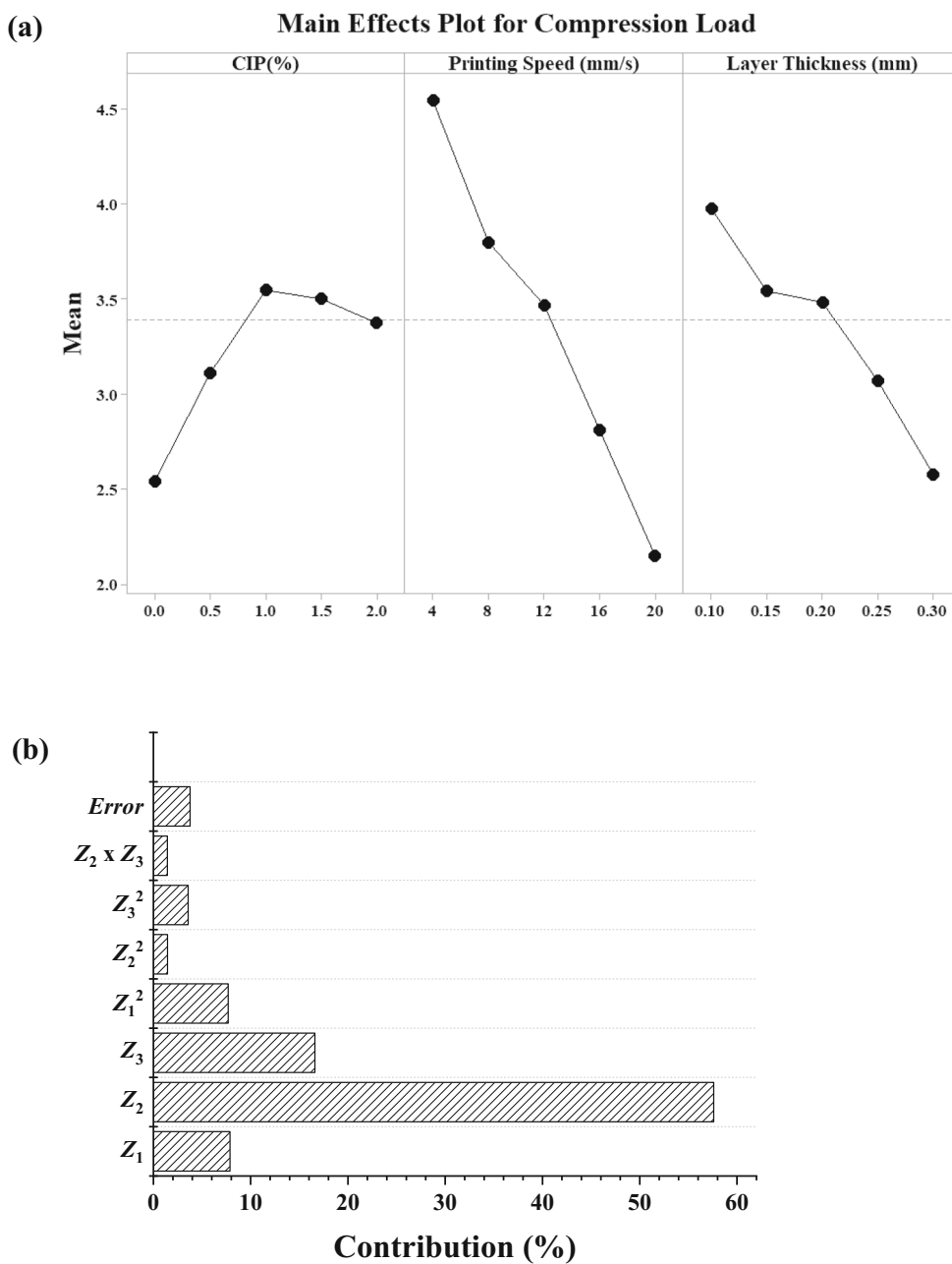

Fig. 11 Printing speed and layer thickness interaction plot on the percentage shrinkage of strut thickness

Fig. 12 a Main effects plot. **b** Percent contribution of each process parameter on radial compression load

(a)

(b)

The slow printing speed provides sufficient time for the joining between the surrounding printed material, which reduces the voids between the layers and provides better mechanical properties [43]. Also, the evaporation of the solvent was slow at slow printing speed, which allows the layers for the better settlement with high bonding strength [16]. However, the strength decreased with increasing the printing speed. The mechanical properties of the stacked macromolecule chain dropped due to lose bonding between the layers. Therefore, the parts printed with 20 mm/s printing speed resulted in minimum compression and flexural properties.

3.3.4 Effect of interactions

Figures 15 and 16 represent the surface 3D and 2D interaction plots between layer thickness and printing speed for R_L and F_L. The layer thickness parameter effect was insignificant for R_L and F_L properties at fast printing speed. The fast-printing speed reduces the material deposition per unit area and provides less time for the homogenous deposition as discussed above. This resulted with both small and large layer thickness values at fast printing speed, which provides the low mechanical properties. Also, the stretching of the filament was higher

Fig. 13 a Main effects plot. **b** Percent contribution of each process parameter on bending load
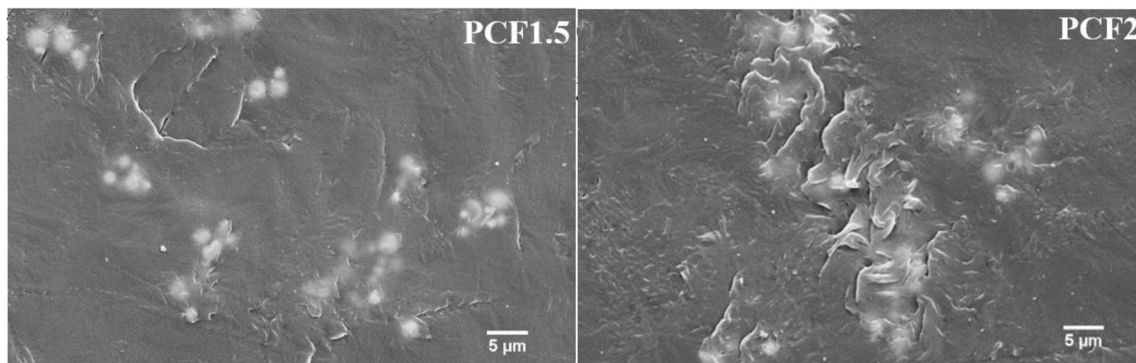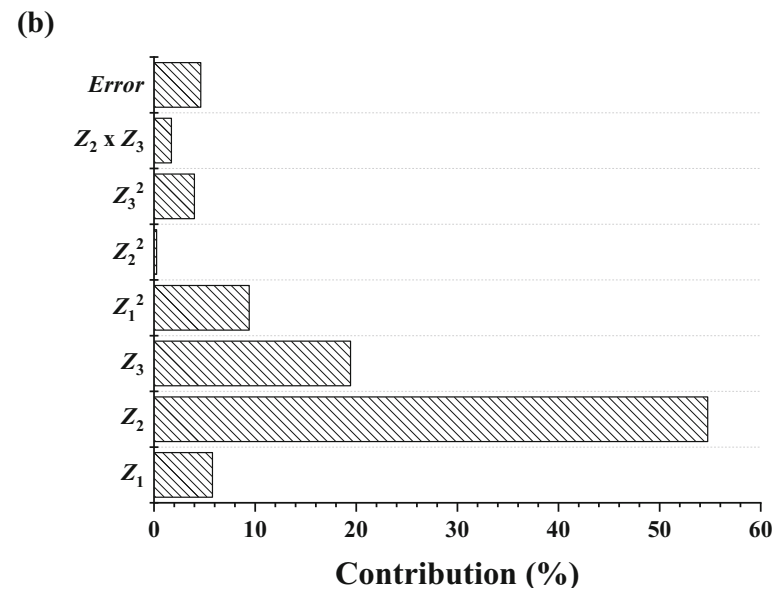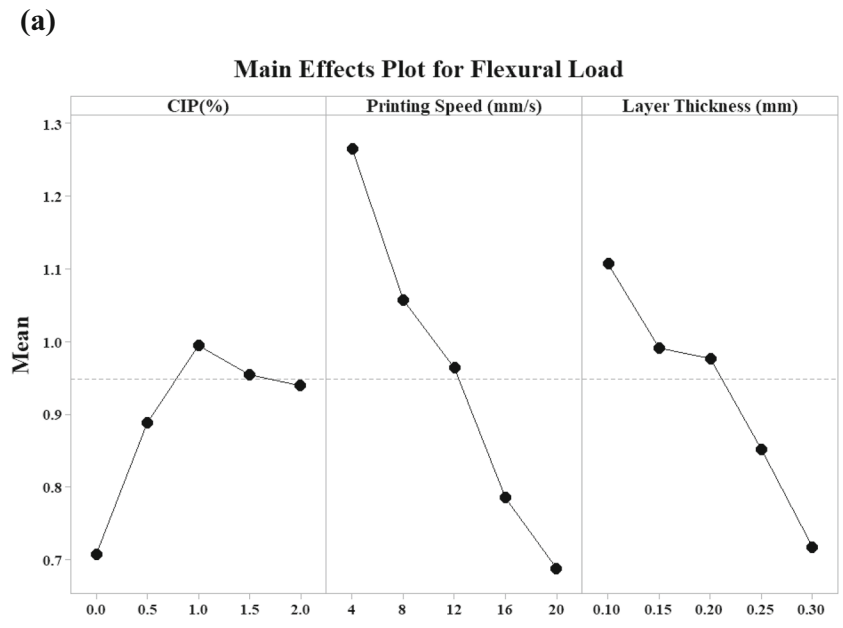
(a)

(b)

Fig. 14 SEM micrograph of polymer composite stents PCF1.5 and PCF2
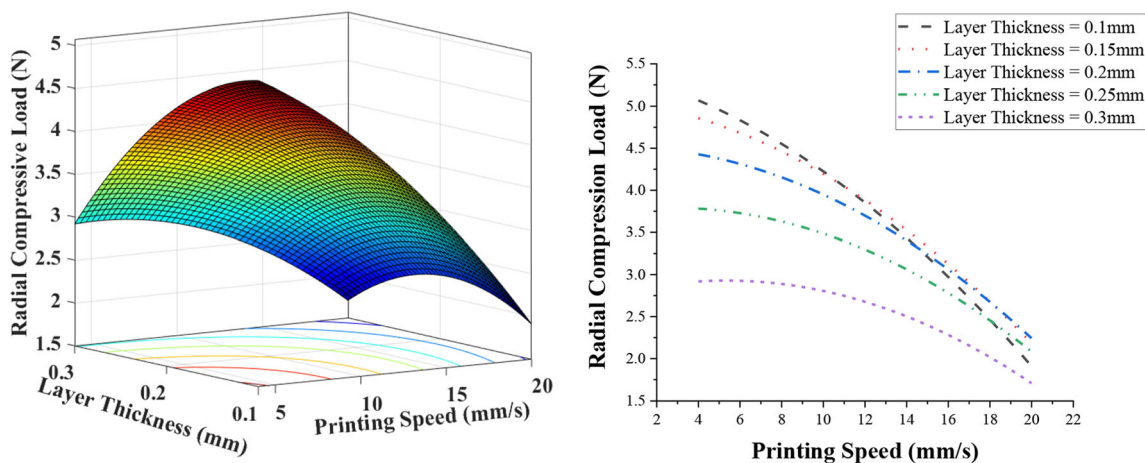
Fig. 15 Printing speed and layer thickness interaction plot on radial compression load

at fast printing speed with high evaporation rate. This results in poor bonding between the layers in respect to any layer thickness value. However, the parts printed with small layer thickness at low printing speed resulted in maximum mechanical strength due to better bonding between the layers as discussed in a previous section.

3.4 Multi-objective optimization

The multi-objective optimization problem was formulated to minimize the w_s, t_s and F_L and maximize the R_L to optimize the process parameters of the developed methodology. The genetic algorithm was employed for multi-objective optimization to determine the globally optimized solution [71]. The Matlab 2015b optimization toolbox was employed to perform multi-objective optimization. The objectives with constraints for optimization are given below.

Minimize : $\varnothing_1 = w_s(\Delta), t_s(\Delta), F_L(\Delta)$ and Maximize $\varnothing_3$

$$= R_L(\Delta)$$

where $\Delta = \{Z_1 Z_2 Z_3\}^T$
Subjected to $0 \leq Z_1 \leq 2, 4 \leq Z_2 \leq 20, 0.1 \leq Z_3 \leq 0.3$

Table 6 describes the determined optimum solution for the multi-objective functions. The efficacy of the present work was evaluated by comparing the various outputs (such as strut thickness and strut width, radial compression load and bending load) with literature regarding the 3D printing of PCL stents. Further, the experiments were performed on the obtained parameters to confirm the results predicted from the optimization technique. The obtained results conformed to the predicted results. The geometry dimension and mechanical properties curves of the fabricated stent at the optimized parameters are shown in Fig. 17.
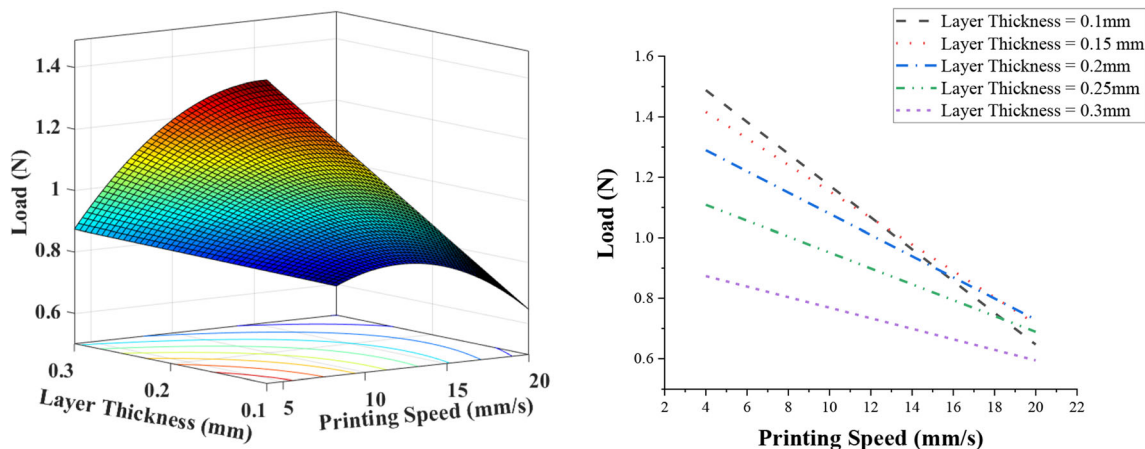

Fig. 16 Printing speed and layer thickness interaction plot on load for bending

Table 6 Optimized response values along with design parameters

S. No.	Z_1	Z_2	Z_3	w_s (%)		t_s (%)		R_L (N)		F_L (N)	
				Statistical	Experimental	Statistical	Experimental	Statistical	Experimental	Statistical	Experimental
1	1.08	8.02	0.20	-12.80 ± 8.18	-13.83	1.90 ± 5.15	1.95	4.12 ± 0.33	3.93	1.13 ± 0.10	1.17

Guerra and Ciurana [72] fabricated the stents with the FDM technique and observed the expansion of the strut width (0.519 mm) as compared to the designed value (0.4 mm), which was very high as observed in the present work (i.e. 0.5 to 0.57 mm). Puppi et al. [22] fabricated a PCL stent by computer-aided wet spinning (CAWS) technique and observed shrinkage in the strut width from 0.35 to 0.318 mm. The radial compression load was 0.317 N and 0.015 N, which was lower than the 3.93 N observed in the current work. Ansari et al. [73] fabricated a PCL tube for vascular application by using the solvent casting method and observed the radial compression load equal to 1.08 N with a wall thickness of 0.3 mm. The present study results outperformed the above-mentioned references. The reinforcement of the CIP particles in PCL has clearly shown the advantage of enhancing mechanical properties in the present work.

Furthermore, to check the distribution of the CIP particles in the fabricated stent at optimized parameters, EDX mapping was conducted (ref. Fig. 18). The distribution of the CIP particles was obtained to be approximately homogenous by the SC-3DP method.

4 Conclusions

In the present study, the process parameters of the solvent cast 3D printing (SC-3DP) technique were analysed for the fabrication of bioresorbable polymer composite stents on the

Fig. 17 a Geometry measurements of strut width and thickness and **b** radial compression and bending load of the sample fabricated at the optimized parameters
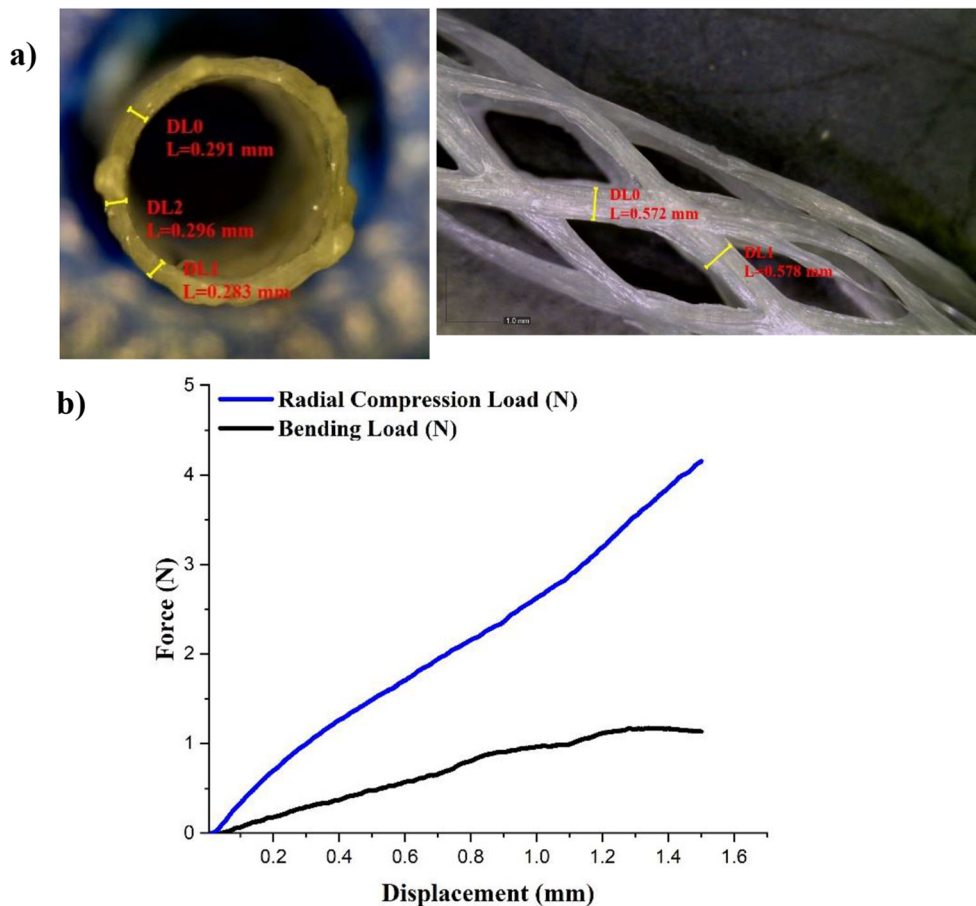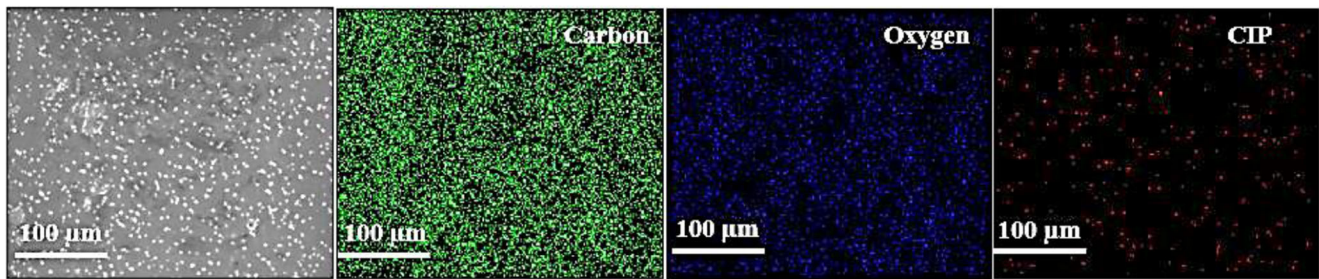
Fig. 18 EDX mapping on the sample fabricated at the optimized parameters

rotating mandrel. The method gives freedom to fabricate interconnected cell shape stents without the support and fabricate polymer-metal composites. Response surface methodology (RSM) was used to develop statistical models, and further multi-objective optimization technique based on genetic algorithm was used to minimize geometry shrinkage and maximize compression properties and flexibility. The various points concluded from the current work are given below:

1. The EDX peaks described the successful reinforcement of CIP in the PCL matrix in the fabricated stents without any contamination.
2. The printing speed and layer thickness were observed as significant factors and having essential contributions over the shrinkage in strut width and strut thickness, radial compression load and flexibility of the polymer composite stents. The higher value of the shrinkage percentage in strut width and strut thickness was observed at a high speed of printing and a small value of the layer thickness. It was due to the stretching and overdeposition of the material by high printing speed.
3. The mechanical properties of the printed stents were also dependent upon the interaction of printing speed and layer thickness. The maximum radial compression load and load for bending were observed at the small layer thickness and slow printing speed.
4. The optimized output responses were found to have − 12.80% shrinkage in strut width, 1.90% shrinkage in strut thickness, 4.12 N radial compression load and 1.13 N load for bending with obtained optimized process parameters such as CIP (%) equal to 1.08%, printing speed equal to 8.02 mm/s and layer thickness equal to 0.2 mm. The low bending load describes the higher flexibility of the stent up to 1.5 mm displacement.

The optimized parameters would be used to fabricate different topological ordered shapes of the stents in the near future. The work would also be extended to the fabrication of patient-specific stents using computer tomography scan data as a case study.

Supplementary Information The online version contains supplementary material available at https://doi.org/10.1007/s00170-021-07423-6.

Author contribution Jasvinder Singh: Conceptualization, methodology, investigation, software, writing and original draft preparation. Gurminder Singh: Conceptualization, supervision, validation and writing (reviewing and editing). Pulak Mohan Pandey: Supervision, visualization and writing (reviewing and editing).

Data availability Not applicable

Code availability Not applicable

Declarations

Competing interests The authors declare no competing interests.

References

1. Gao P, Wang D, Zhao Z, Cai Y, Li T, Shi H, Wu W, He W, Yin L, Huang S, Zhu F, Jiao L, Ji X, Qureshi AI, Ling F (2016) Multicenter prospective trial of stent placement in patients with symptomatic high-grade intracranial stenosis. Am J Neuroradiol 37:1275–1280. https://doi.org/10.3174/ajnr.A4698
2. Nikoubashman O, Heringer S, Feher K, et al (2018) Development of a polymer-based biodegradable neurovascular stent prototype: a preliminary in vitro and in vivo study. Macromol Biosci 18:1–6. https://doi.org/10.1002/mabi.201700292
3. Omar WA, Kumbhani DJ (2019) The current literature on bioabsorbable stents: a review. Curr Atheroscler Rep 21:1–9
4. Zhao D, Zhou R, Sun J, Li H, Jin Y (2019) Experimental study of polymeric stent fabrication using homemade 3D printing system. Polym Eng Sci 59:1122–1131. https://doi.org/10.1002/pen.25091
5. Ni L, Chen H, Luo Z, Yu Y (2020) Bioresorbable vascular stents and drug-eluting stents in treatment of coronary heart disease: a meta-analysis. J Cardiothorac Surg 15:1–7. https://doi.org/10.1186/s13019-020-1041-5
6. Vroman I, Tighzert L, Vroman I, Tighzert L (2009) Biodegradable polymers. Materials (Basel) 2:307–344. https://doi.org/10.3390/ma2020307
7. Sivalingam G, Madras G (2003) Thermal degradation of poly (ε-caprolactone). Polym Degrad Stab 80:11–16. https://doi.org/10.1016/S0141-3910(02)00376-2
8. Gupta KK, Kundan A, Mishra PK, Srivastava P, Mohanty S, Singh NK, Mishra A, Maiti P (2012) Polycaprolactone composites with TiO₂ for potential nanobiomaterials: tunable properties using different phases. Phys Chem Chem Phys 14:12844–12853. https://doi.org/10.1039/c2cp41789h

9. Xu J, Zhang Y, Feng YB, Qiu T, Wang G, Liu R (2018) Electromagnetic and mechanical properties of carbonyl iron powder-filled methyl vinyl silicone rubber during thermal aging. Polym Compos 39:2897–2903. https://doi.org/10.1002/pc.24286

10. Teresa R, Antonio G, Vincenzo D'A et al (2010) Poly(ε-caprolactone) reinforced with sol-gel synthesized organic-inorganic hybrid fillers as composite substrates for tissue engineering. J Appl Biomater Biomech 8:146–152. https://doi.org/10.5301/JABB.2010.6094

11. Singh H, Sodhi GPS, Singh M, Chelliah NM, Singh H (2019) Study: wear and superhydrophobic behaviour of PTFE-ceria composite. Surf Eng 35:550–556. https://doi.org/10.1080/02670844.2018.1499176

12. Vella JB, Trombetta RP, Hoffman MD, Inzana J, Awad H, Benoit DSW (2018) Three dimensional printed calcium phosphate and poly(caprolactone) composites with improved mechanical properties and preserved microstructure. J Biomed Mater Res Part A 106:663–672. https://doi.org/10.1002/jbm.a.36270

13. Zhang J, Feng Y, Qiu T, Tang C (2014) Preparation and characterization of carbonyl iron powder/millable polyurethane elastomer microwave absorbing patch. Polym Compos 35:1318–1324. https://doi.org/10.1002/pc.22782

14. Liu B, Zheng YF (2011) Effects of alloying elements (Mn, Co, Al, W, Sn, B, C and S) on biodegradability and in vitro biocompatibility of pure iron. Acta Biomater 7:1407–1420. https://doi.org/10.1016/j.actbio.2010.11.001

15. Peuster M, Wohlsein P, Brügmann M, Ehlerding M, Seidler K, Fink C, Brauer H, Fischer A, Hausdorf G (2001) A novel approach to temporary stenting: degradable cardiovascular stents produced from corrodible metal-results 6-18 months after implantation into New Zealand white rabbits. Heart 86:563–569. https://doi.org/10.1136/heart.86.5.563

16. Singh J, Pandey PM, Kaur T, Singh N (2021) A comparative analysis of solvent cast 3D printed carbonyl iron powder reinforced polycaprolactone polymeric stents for intravascular applications. J Biomed Mater Res - Part B Appl Biomater 1–16. doi:https://doi.org/10.1002/jbm.b.34795

17. Devasthali SD, Gordeuk VR, Brittenham GM et al (1991) Bioavailability of carbonyl iron: a randomized, double-blind study. Eur J Haematol 46:272–278

18. Cvek M, Mrlik M, Ilcikova M, Plachy T, Sedlacik M, Mosnacek J, Pavlinek V (2015) A facile controllable coating of carbonyl iron particles with poly(glycidyl methacrylate): a tool for adjusting MR response and stability properties. J Mater Chem C 3:4646–4656. https://doi.org/10.1039/c5tc00319a

19. Singh J, Kaur T, Singh N, Pandey PM (2020) Biological and mechanical characterization of biodegradable carbonyl iron powder/polycaprolactone composite material fabricated using three-dimensional printing for cardiovascular stent application. Proc Inst Mech Eng Part H J Eng Med 234:975–987. https://doi.org/10.1177/0954411920936055

20. Guerra AJ, Ciurana J (2018) Stent's manufacturing field: past, present, and future prospects. In: Angiography. IntechOpen, pp 1–20. https://doi.org/10.5772/intecopen.81668

21. Stepak B, Antończak AJ, Bartkowiak-Jowsa M et al (2014) Fabrication of a polymer-based biodegradable stent using a CO_2 laser. Arch Civ Mech Eng 14:317–326. https://doi.org/10.1016/j.acme.2013.08.005

22. Puppi D, Pirosa A, Lupi G, Erba PA, Giachi G, Chiellini F (2017) Design and fabrication of novel polymeric biodegradable stents for small caliber blood vessels by computer-aided wet-spinning. Biomed Mater 12:12. https://doi.org/10.1088/1748-605X/aa6a28

23. Singh S, Singh G, Prakash C, Ramakrishna S (2020) Current status and future directions of fused filament fabrication. J Manuf Process 55:288–306. https://doi.org/10.1016/j.jmapro.2020.04.049

24. Singh G, Pandey PM (2020) Role of imaging data in additive manufacturing for biomedical applications. In: 3D printing in biomedical engineering. pp 69–94

25. van Lith R, Baker E, Ware H, Yang J, Farsheed AC, Sun C, Ameer G (2016) 3D-printing strong high-resolution antioxidant bioresorbable vascular stents. Adv Mater Technol 1:1–7. https://doi.org/10.1002/admt.201600138

26. Flege C, Vogt F, Höges S, Jauer L, Borinski M, Schulte VA, Hoffmann R, Poprawe R, Meiners W, Jobmann M, Wissenbach K, Blindt R (2013) Development and characterization of a coronary polylactic acid stent prototype generated by selective laser melting. J Mater Sci Mater Med 24:241–255. https://doi.org/10.1007/s10856-012-4779-z

27. Guerra AJ, Cano P, Rabionet M, Puig T, Ciurana J (2018) 3D-printed PCL/PLA composite stents: towards a new solution to cardiovascular problems. Materials (Basel) 11:1–13. https://doi.org/10.3390/ma11091679

28. Singh G, Missiaen JM, Bouvard D, Chaix JM (2021) Copper extrusion 3D printing using metal injection moulding feedstock: analysis of process parameters for green density and surface roughness optimization. Addit Manuf 38:101778. https://doi.org/10.1016/j.addma.2020.101778

29. Wang C, Zhang L, Fang Y, Sun W (2020) Design, characterization, and 3d printing of cardiovascular stents with zero Poisson's ratio in longitudinal deformation. Engineering 1–12. https://doi.org/10.1016/j.eng.2020.02.013

30. Guo SZ, Gosselin F, Guerin N, Lanouette AM, Heuzey MC, Therriault D (2013) Solvent-cast three-dimensional printing of multifunctional microsystems. Small 9:4118–4122. https://doi.org/10.1002/smll.201300975

31. Singh J, Pandey PM, Kaur T, Singh N (2020) Surface characterization of polycaprolactone and carbonyl iron powder composite fabricated by solvent cast 3D printing for tissue engineering. Polym Compos 1–7. doi:https://doi.org/10.1002/pc.25871, 42, 865, 871

32. Qiu T, Jiang W, Yan P, Jiao L, Wang X (2020) Development of 3D-printed sulfated chitosan modified bioresorbable stents for coronary artery disease. Front Bioeng Biotechnol 8:1–12. https://doi.org/10.3389/fbioe.2020.00462

33. Jia H, Gu S-Y, Chang K (2018) 3D printed self-expandable vascular stents from biodegradable shape memory polymer. Adv Polym Technol 37:3222–3228. https://doi.org/10.1002/adv.22091

34. Xu Z, Li Z, Shi J et al (2018) 3D printing and characterization of the biodegradable vascular stent. Int J Comput Electr Eng 10:254–264. https://doi.org/10.17706/ijcee.2018.10.4.254-264

35. Xu C, Bouchemit A, Rance E et al Solvent-cast based metal 3D printing and secondary metallic infiltration. J Mater Chem C 5:10448. https://doi.org/10.1039/c7tc02884a

36. Singh J, Singh G, Pandey PM (2021) Additive manufacturing of functionalized nanomaterials for the modern health care industry. In: Additive manufacturing with functionalized nanomaterials, 1st Edition. pp 55–85

37. ASTM F2081 - 06(2017) Standard Guide for Characterization and Presentation of the Dimensional Attributes of Vascular Stents 1. In: ASTM Int

38. Cabrera MS, Oomens CWJ, Baaijens FPT (2017) Understanding the requirements of self-expandable stents for heart valve replacement: radial force, hoop force and equilibrium. J Mech Behav Biomed Mater 68:252–264. https://doi.org/10.1016/j.jmbbm.2017.02.006

39. Al Suwaidi J (2000) Coronary artery stents. JAMA 284:1828–1836. https://doi.org/10.1001/jama.284.14.1828

40. Singh G, Pandey PM (2019) Uniform and graded copper open cell ordered foams fabricated by rapid manufacturing: surface morphology, mechanical properties and energy absorption capacity. Mater

Sci Eng A 761:138035. https://doi.org/10.1016/j.msea.2019.138035

41. Sharma P, Pandey PM (2018) Morphological and mechanical characterization of topologically ordered open cell porous iron foam fabricated using 3D printing and pressureless microwave sintering. Mater Des 160:442–454. https://doi.org/10.1016/j.matdes.2018.09.029

42. Singh J, Singh G, Pandey PM (2020) Electric discharge machining using rapid manufactured complex shape copper electrode with cryogenic cooling channel. Proc Inst Mech Eng Part B J Eng Manuf 1–13. doi:https://doi.org/10.1177/0954405420949102, 235, 173, 185

43. Kim D. B, Choi H, Joo SM et al (2013) A comparative reliability and performance study of different stent designs in terms of mechanical properties: foreshortening, recoil, radial force, and flexibility. Artif Organs 37:368–379. https://doi.org/10.1111/aor.12001

44. ASTM F2606 (2018) Standard guide for three-point bending of balloon expandable vascular stents. ASTM Int 08:1–6. https://doi.org/10.1520/F2606-08R14.2.1.4

45. Jin Y, Zhao D, Huang Y (2018) Study of extrudability and standoff distance effect during nanoclay-enabled direct printing. Bio-Design Manuf 1:123–134. https://doi.org/10.1007/s42242-018-0009-y

46. Guo SZ, Heuzey MC, Therriault D (2014) Properties of polylactide inks for solvent-cast printing of three-dimensional freeform microstructures. Langmuir 30:1142–1150. https://doi.org/10.1021/la4036425

47. Farzadi A, Solati-Hashjin M, Asadi-Eydivand M, Osman NAA (2014) Effect of layer thickness and printing orientation on mechanical properties and dimensional accuracy of 3D printed porous samples for bone tissue engineering. PLoS One 9:e108252. https://doi.org/10.1371/journal.pone.0108252

48. Geng P, Zhao J, Wu W, Ye W, Wang Y, Wang S, Zhang S (2019) Effects of extrusion speed and printing speed on the 3D printing stability of extruded PEEK filament. J Manuf Process 37:266–273. https://doi.org/10.1016/j.jmapro.2018.11.023

49. Vaezi M, Chua CK (2011) Effects of layer thickness and binder saturation level parameters on 3D printing process. Int J Adv Manuf Technol 53:275–284. https://doi.org/10.1007/s00170-010-2821-1

50. Christiyan KGJ, Chandrasekhar U, Venkateswarlu K (2016) A study on the influence of process parameters on the mechanical properties of 3D printed ABS composite. IOP Conf Ser Mater Sci Eng 114:012109. https://doi.org/10.1088/1757-899X/114/1/012109

51. Singh H, Kumar D, Singh H (2021) Development of magnesium-based hybrid metal matrix composite through in situ micro, nano reinforcements. J Compos Mater 55:109–123. https://doi.org/10.1177/0021998320946432

52. Pandey A, Singh G, Singh S, Jha K, Prakash C (2020) 3D printed biodegradable functional temperature-stimuli shape memory polymer for customized scaffoldings. J Mech Behav Biomed Mater 108:103781. https://doi.org/10.1016/j.jmbbm.2020.103781

53. Singh G, Pandey PM (2019) Rapid manufacturing of copper components using 3D printing and ultrasonic assisted pressureless sintering: experimental investigations and process optimization. J Manuf Process 43:253–269. https://doi.org/10.1016/j.jmapro.2019.05.010

54. Singh G, Singh S, Singh J, Pandey PM (2020) Parameters effect on electrical conductivity of copper fabricated by rapid manufacturing. Mater Manuf Process 00:1–12. https://doi.org/10.1080/10426914.2020.1784937

55. Berrocal DH, González GE, Fernández A, Perez S, Wilensky L, Morales C, Grinfeld L, Gelpi RJ (2008) Effects of overexpansion on stents' recoil, symmetry/asymmetry, and neointimal hyperplasia in aortas of hypercholesterolemic rabbits. Cardiovasc Pathol 17:289–296. https://doi.org/10.1016/j.carpath.2007.10.005

56. Azevedo MC, Reis RL, Claase MB, Grijpma DW, Feijen J (2003) Development and properties of polycaprolactone/hydroxyapatite composite biomaterials. J Mater Sci Mater Med 14:103–107. https://doi.org/10.1023/A:1022051326282

57. Ahmad AF, Abbas Z, Aziz SA, Obaiys SJ, Zainuddin MF (2018) Synthesis and characterisation of nickel oxide reinforced with polycaprolactone composite for dielectric applications by controlling nickel oxide as a filler. Results Phys 11:427–435. https://doi.org/10.1016/J.RINP.2018.08.041

58. Ren L, Zhou X, Song Z, Zhao C, Liu Q, Xue J, Li X (2017) Process parameter optimization of extrusion-based 3D metal printing utilizing PW-LDPE-SA binder system. Materials (Basel) 10. 10. https://doi.org/10.3390/ma10030305

59. Ketelaars AAJ, Papantoniou Y, Nakayama K (1997) Analysis of the density and the enthalpy of poly(ε-caprolactone)-polycarbonate blends: amorphous phase compatibility and the effect of secondary crystallization. 921–927

60. Gorodkin SR, James RO, Kordonski WI (2009) Magnetic properties of carbonyl iron particles in magnetorheological fluids. J Phys Conf Ser 149:012051. https://doi.org/10.1088/1742-6596/149/1/012051

61. Huang B, Bártolo PJ (2018) Rheological characterization of polymer/ceramic blends for 3D printing of bone scaffolds. Polym Test 68:365–378. https://doi.org/10.1016/j.polymertesting.2018.04.033

62. Jin Y, Chai W, Huang Y (2017) Printability study of hydrogel solution extrusion in nanoclay yield-stress bath during printing-then-gelation biofabrication. Mater Sci Eng C 80:313–325. https://doi.org/10.1016/j.msec.2017.05.144

63. Ciurana J De Guerra A, Roca A, Ciurana J De (2017) A novel 3D additive manufacturing machine to biodegradable stents. Procedia Manuf 13:718–723

64. Lee JM, Yeong WY (2015) A preliminary model of time-pressure dispensing system for bioprinting based on printing and material parameters: this paper reports a method to predict and control the width of hydrogel filament for bioprinting applications. Virtual Phys Prototyp 10:3–8. https://doi.org/10.1080/17452759.2014.979557

65. Kang X B, Shen C, Qiu T, Feng Y B (2007) Study of mechanical properties of RTV silicone sealant modified by carbonyl iron powder. J Mater Sci Eng 25:99–101

66. Jing Q, Law JY, Tan LP, Silberschmidt VV, Li L, Dong ZL (2015) Preparation, characterization and properties of polycaprolactone diol-functionalized multi-walled carbon nanotube/thermoplastic polyurethane composite. Compos Part A Appl Sci Manuf 70:8–15. https://doi.org/10.1016/j.compositesa.2014.10.028

67. Haq Abdul R, Saidin M, Uzir Wahit M (2013) Improvement of mechanical properties of polycaprolactone (PCL) by addition of nano-montmorillonite (MMT) and hydroxyapatite (HA). Appl Mech Mater 315:815–819. https://doi.org/10.4028/ww.scientific.net/AMM.315.815

68. De Santis R, Gloria A, Russo T et al (2011) A basic approach toward the development of nanocomposite magnetic scaffolds for advanced bone tissue engineering. J Appl Polym Sci 122:3599–3605. https://doi.org/10.1002/app.34771

69. Uddin MS, Sidek MFR, Faizal MA, Ghomashchi R, Pramanik A (2017) Evaluating mechanical properties and failure mechanisms of fused deposition modeling acrylonitrile butadiene styrene parts. J Manuf Sci Eng Trans ASME 139:139. https://doi.org/10.1115/1.4036713

70. Wang P, Zou B, Ding S et al (2020) Effects of FDM-3D printing parameters on mechanical properties and microstructure of CF/PEEK and GF/PEEK. Chin J Aeronaut. https://doi.org/10.1016/j.cja.2020.05.040

71. Konak A, Coit DW, Smith AE (2006) Multi-objective optimization using genetic algorithms: a tutorial. Reliab Eng Syst Saf 91:992–1007. https://doi.org/10.1016/j.ress.2005.11.018

72. Guerra AJ, Ciurana J (2018) 3D-printed bioabsordable polycaprolactone stent: the effect of process parameters on its physical features. Mater Des 137:430–437. https://doi.org/10.1016/j.matdes.2017.10.045

73. Ansari M, Golzar M, Baghani M, Taghavimehr M (2020) An experimental investigation on shape memory polymer and metallic stents under bending and radial compression. Eng Res Express 2:1–9